LASER & PHOTONICS REVIEWS

www.lpr-journal.org

Gauge-Induced Floquet Topological States in Photonic Waveguides

*Wange Song, Yuxin Chen, Hanmeng Li, Shenglun Gao, Shengjie Wu, Chen Chen, Shining Zhu, and Tao Li**

Tremendous efforts are devoted to the research of exotic photonic topological states, in which Floquet systems suggest new engineered topological phases and provide a powerful tool to manipulate the optical fields. Here, a gauge-induced topological state localized at the interface between two gauge-shifted Floquet photonic lattices with the same topological order is demonstrated. The quasienergy band structures reveal that these interface modes belong to the Floquet π modes, which are further found to enable an asymmetric topological transport of this interface mode thanks to the flexible control of the Floquet gauge. The intriguing propagations of the gauge-induced topological states are experimentally verified in a silicon waveguides platform at near-infrared wavelengths, which show broadband working wavelengths and robustness against the structural fluctuations. This work provides a new route in manipulating optical topological modes by Floquet engineering and inspires more possibilities in photonics integrations.

1. Introduction

Topological photonics has provided unprecedented opportunities for optical field manipulations.[1,2] Tremendous progress has been made exploring the unique properties of photonic topological states and utilizing the topological protection against disorder to design robust photonic devices. For example, high-order topological insulators,[3–5] non-Hermitian topological steering,[6–8] and topological lasers.[9–11] Specifically, the Su–Schrieffer–Heeger (SSH) model is a popular model revealing nontrivial topology in one-dimensional (1D) systems,[12] in which the chiral zero modes exhibit robustness against local structural fluctuations and disorders that plays an important role in light transport,[13–15] lasing,[16,17] and photonic integration,[18–20] etc. Recently, the notion of topological phases has been extended to Floquet systems where the Hamiltonian is periodic in time, $H(t + T) = H(t)$, with T is the driving period.[21–26] Periodically driving the SSH models provides a powerful tool to engineer the quasienergy band structure and induces new topologically nontrivial phases with the emergence of anomalous Floquet topological states (i.e., π modes).[27–30] In contrast to the static zero modes, the π modes exhibit periodic oscillation features. Thanks to the flexibility of Floquet engineering, the topological properties of Floquet systems are much richer than static systems. Unconventional effects have been demonstrated by tuning the driving frequency and amplitude, such as anomalous topological Floquet edge modes,[30–32] "0" and "π" Majorana modes,[33,34] and interacting topological Floquet phases.[35,36] Importantly, the Floquet systems also enable the manipulations of artificial gauge fields (i.e., the Floquet gauge).[37,38]

As an important concept in physics, artificial gauge fields govern the effective dynamics of neutral particles (i.e., photons). It can be generated by properly engineering a physical system through the geometric design or external modulations, which allows us to endow systems with a wide range of intriguing features and novel functions, such as effective magnetic field for photons,[39,40] photonic topological insulators,[41,42] dynamic localization and self-imaging,[43–45] and light guiding.[46,47] Therefore, it is quite possible to engineering the Floquet gauge to access new emergent topological effects and potential applications.

Here, we demonstrate a gauge-induced photonic topological state, which forms at the interface between two lattices with different Floquet gauges. We use lattices of curved silicon waveguides array as a platform to implement the Floquet engineering, where the gauge-induced π modes can be constructively controlled by the Floquet gauge. It therefore gives rise to asymmetric topological transports by Floquet gauge engineering. Inheriting the topological protection property, these new modes and asymmetric topological transport show good robustness against the structure fluctuations and broad working bandwidth, suggesting application potentials in photonic integrations.

W. Song, Y. Chen, H. Li, S. Gao, S. Wu, C. Chen, Prof. S. Zhu, Prof. T. Li
National Laboratory of Solid State Microstructures
Key Laboratory of Intelligent Optical Sensing and Manipulation
Jiangsu Key Laboratory of Artificial Functional Materials
College of Engineering and Applied Sciences
Nanjing University
Nanjing 210093, China
E-mail: taoli@nju.edu.cn

W. Song, Y. Chen, H. Li, S. Gao, S. Wu, C. Chen, Prof. S. Zhu, Prof. T. Li
Collaborative Innovation Center of Advanced Microstructures
Nanjing 210093, China

The ORCID identification number(s) for the author(s) of this article can be found under https://doi.org/10.1002/lpor.202000584

DOI: 10.1002/lpor.202000584

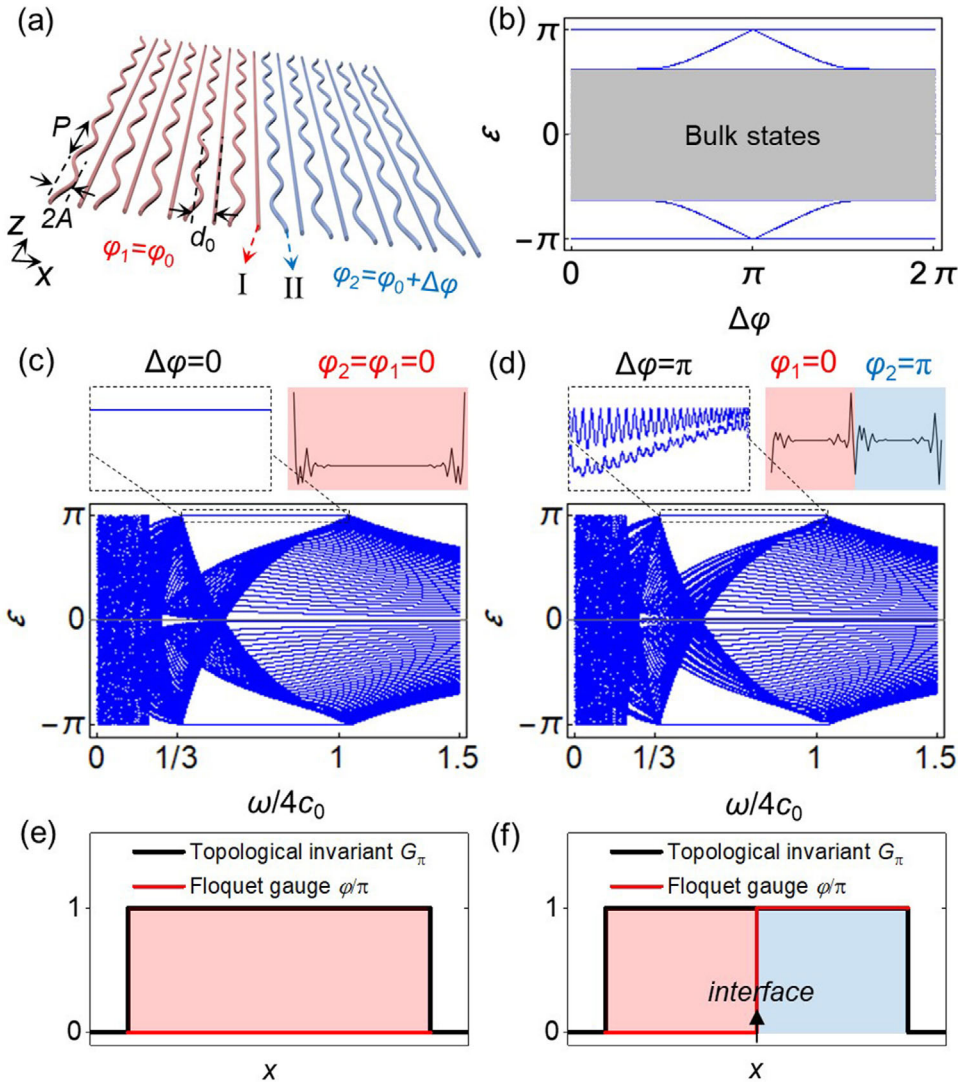

Figure 1. Gauge-induced photonic π-interface modes. a) Schematics of 1D periodically driven waveguide array consists of two arrays with the same topological phases but different Floquet gauge. b) Corresponding quasienergies with $\omega/4c_0 = 0.4$ under open boundary conditions with 80 waveguides as a function of gauge difference $\Delta\varphi$. A new pair of π modes that localized at the gauge-shifted interface forms at $\Delta\varphi = \pi$. c,d) Quasienergies as a function of ω with $\Delta\varphi = 0$ c) and $\Delta\varphi = \pi$ d). The two insets show the zoom-in of quasienergies and field distributions of the Floquet π modes. e,f) Calculated topological invariant G_π at $\omega/4c_0 = 0.4$ and Floquet gauge φ across the waveguide array for $\Delta\varphi = 0$ e) and $\Delta\varphi = \pi$ f). The arrow in f) indicates the gauge-shifted interface.

2. Results

2.1. Photonic π-Interface Modes Induced by Floquet Gauge Transition

The basic idea of gauge-induced topological mode can be illustrated by a simple example of a 1D SSH model with Floquet engineering,[27–30] as the schematic depicted in **Figure 1**a. Every other waveguide is periodically bent along their propagating direction z, i.e., $x_0(z) = A\cos(\omega z + \varphi)$, where z acts as the synthetic time dimension,[41] A and ω ($\omega \equiv 2\pi/P$, P is the period) denote the amplitude and frequency of the sinusoidal bending, and φ is the initial phase determined by the starting "time" $z = 0$, i.e., Floquet gauge.[37,38] Two arrays with different Floquet gauge ($\varphi_1 = \varphi_0$ at left and $\varphi_2 = \varphi_1 + \Delta\varphi$ at right, shown in Figure 1a) are combined and form an interface as $\Delta\varphi \neq 0$. The waveguides on both sides of the interface are marked by I and II. Here, we need to mention that our Floquet modulation is not based on the commonly used purely curved waveguides, but a straight and curved alternating arrangement. It provides a continuous tuning of the Floquet gauge difference ($\Delta\varphi$) across the interface with exact sine/cosine function, because the interface is composed of a pair of straight and curved waveguides (i.e., I and II indicated in Figure 1a). It guarantees a well-defined periodic coupling as required by the Floquet theory, while an interface composed of two shifted curved waveguides will break this definition and leads to more complex coupling circumstances. Our design enables us to apply flexible controls on the Floquet gauge, which

is necessary to inspect possible anomalous topological effects. Through the coupled-mode theory (CMT), the waveguide array can be mapped into an effective 1D time-periodic tight-binding-approximated Hamiltonian as

$$H(z) = \sum_{n=1,3,5,\ldots}^{2N-1} \beta_n(z) a_n^{\dagger} a_n + \sum_{n=2,4,6\ldots}^{2N} \beta_0 a_n^{\dagger} a_n + \sum_{n=1}^{N-1} [c_0 + (-1)^n \delta c_1(z)] a_n^{\dagger} a_{n+1} + \sum_{n=N}^{2N-1} [c_0 + (-1)^n \delta c_2(z)] a_n^{\dagger} a_{n+1} + H.c. \quad (1)$$

Here, $a_n^{\dagger}$ and a_n are the creation and annihilation operators at the nth waveguide, N is the number of waveguides of each array (N is even), the total waveguides number are $2N$, β_0 is the propagation constant for the straight waveguides, and $\beta_n(z)$ is the effective propagation constant for the curved waveguides which can be treated as a constant in the weak-guidance approximation (WGA).[49] The third and fourth terms in Equation (1) represent couplings between nearest-neighbor (NN) waveguides for the left and right arrays with a constant (staggered) coupling strength $c_0(\delta c(z))$. According to the WGA, the NN coupling strength mainly depends on their distance $d(z)$. In our configuration, the NN spacing $d_{1(2)}$ for left (right) arrays (center-to-center distance) $d_{1(2)}(z) = d_0 \pm A\cos(\omega z + \varphi_{1(2)})$, where d_0 is the spacing without bending. Consequently, c can be approximated as $c_{1(2)}(z) = c_0 \pm \delta c \cos(\omega z + \varphi_{1(2)})$. Note that the staggered term $\delta c_{1(2)}(z)$ is periodically modulated, and the Hamiltonian $H(z)$ in Equation (1) thus exactly mimics the periodically driven SSH model with tunable time-periodic NN couplings and Floquet gauge modulations. According to the Floquet theory, the evolution of our system with Hamiltonian $H(z)$ is governed by the time evolution operator $U(z) = \hat{T} e^{-i\int_0^z H(z')dz'}$, where $\hat{T}$ denotes the time-ordering operator. The Floquet operator is defined as the time evolution operator for one full period P, given by $U(P)$, from which a time-averaged effective Hamiltonian can be defined as $H_{\text{eff}} = (i/P)\ln U(P)$.[21] The eigenvalues of H_{eff} correspond to the quasienergy spectrum of the system.

We first consider $\Delta\varphi = 0$, in which the array as a whole exhibits no Floquet gauge transition. Figure 1c shows the quasienergy (ϵ) spectrum of 80 waveguides under open-boundary conditions. A Z-valued invariant G_{π} can be defined for the quasienergy spectrum of this systems [29,30] (see Section S1 in the Supporting Information). The driving frequency ω determines the topological phases: $\omega/4c_0 > 1$ gives rise to $G_{\pi} = 0$ and corresponds to the topologically trivial phase, whereas $1/3 < \omega/4c_0 < 1$ gives rise to $G_{\pi} = 1$ and corresponds to the nontrivial phase that supports topological π modes, as verified by the quasienergy spectrum (see Figure 1c). As an example, the system of $\omega/4c_0 = 0.4$ shows nontrivial topological phase across the whole system (see Figure 1e) with localized edge modes on two boundaries (see inset figures of Figure 1c). Interestingly, when Floquet gauges of the two arrays are different, especially, anti-phased ($\Delta\varphi = \pi$), new π modes would emerge with localized fields at the gauge transition interface. Figure 1b displays the quasienergy spectrum at $\omega/4c_0 = 0.4$ as a function of gauge difference $\Delta\varphi$, where two new discrete modes stand out from bulk modes and gradually turn into π modes as $\Delta\varphi$ reaches π, while the original π modes keep unchanged. Figure 1d shows the quasienergy spectrum with $\Delta\varphi = \pi$, and π modes also appear within the range $1/3 < \omega/4c_0 < 1$. After careful observation, one indeed finds an additional pair of π modes in this range (see the zoom-in figure in Figure 1d). The new π modes have strong localizations at the gauge transition interface, as shown in the inset of Figure 1d. We note that the two arrays have the same topological order defined by G_{π}, despite the change of Floquet gauge (see Figure 1f). Without loss of generality, φ_0 is set as 0 here, which is not crucial to the existence of the new π modes (see Section S1 in the Supporting Information).

2.2. Simulation and Experimental Results

To observe the formation of these gauge-induced interface modes, we excite an interface waveguide (e.g., waveguide-I) of the systems composed of 80 waveguides and investigate the dynamics of light. **Figure 2**d–f shows the theoretical (CMT) results (left panels) corresponding to different gauge difference $\Delta\varphi$ with a fixed $\varphi_0 = 0$. At $\Delta\varphi = 0$ without gauge transition, the optical fields spread out into the bulk of the lattices, indicating no localized modes at the interface. By contrast, as the $\Delta\varphi$ increases, bulk diffraction is suppressed and the optical field gradually tends to be localized at the interface and finally get trapped at the interface at $\Delta\varphi = \pi$. It is evident that the π-interface modes form with the Floquet gauge transition. Afterward, we carried out full-wave simulations (COMSOL MULTIPHYSICS) and experiments in a silicon waveguide array on a sapphire substrate. The structural parameters of waveguide width (w) and height (h) are optimized as $w = 400$ nm, $h = 220$ nm to support only one fundamental mode in the silicon waveguide at $\lambda = 1550$ nm with a propagation constant $\beta_0 = 2.1601k_0$ (k_0 is the free space k-vector). To realize the periodically driven condition, we consider that the silicon waveguide is sinusoidally curved along the propagation direction z as $x_0(z) = A\cos(2\pi z/P + \varphi)$, where $A = 71.5$ nm, $P = 48.4$ μm. Note that the bending period P is larger than about three orders of magnitude over the amplitude A, which leads to a negligible loss for silicon waveguides that have well-confined modes due to the quite large refractive index. The spacing of neighboring waveguides without bending $d_0 = 618.5$ nm. Based on these designs, the coupling coefficient approximately follows $c(z) = c_0 \pm \delta c\cos(2\pi z/P + \varphi)$, where $c_0 = 0.0811\ \mu\text{m}^{-1}$, $\delta c = 0.0405\ \mu\text{m}^{-1}$, and $\omega = 0.130\ \mu\text{m}^{-1}$, corresponding to the theoretical calculations. The schematics of the silicon waveguide array and the zoom-in input ends for different $\Delta\varphi$ are presented in Figure 2a,b, respectively. Figure 2d–f (middle panels) shows the simulated optical field evolutions of different $\Delta\varphi$ for 20 waveguides and 100 μm propagations, corresponding to the CMT calculation enclosed by dashed boxes in the left panels. Since the full-wave simulation is quite time-consuming, we didn't perform simulations over a same large scale as the CMT calculations. Nevertheless, the simulated results are in extremely good agreement with the CMT results and clearly demonstrate the gauge transition induced π-interface modes.

The experimental samples were fabricated by E-beam lithography and inductively coupled plasma (ICP) etching process (see

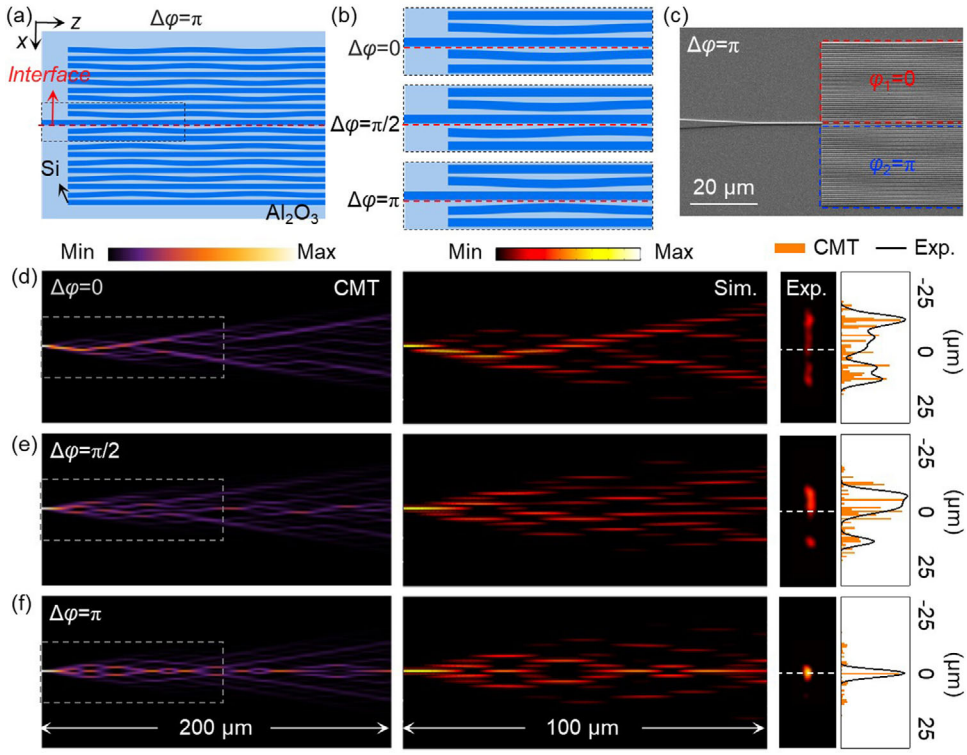

Figure 2. Observation of gauge-induced topological dynamics. a) Schematics of the silicon waveguide array, where the interface is indicated by the red dashed line. b) Zoom-in figure of the input end for different $\Delta\varphi$. c) SEM image of the fabricated sample with $\Delta\varphi = \pi$. d–f) Field evolutions with different $\Delta\varphi$. Left panel: CMT calculated field evolutions; middle panel: simulation results within the boxed region in the left panel; right panel: experimental results with output intensity profiles. The π-interface modes form when $\Delta\varphi$ increase from 0 to π. Here, $\varphi_0 = 0$. The white dashed lines in experiment results indicate the interface.

the Experimental Section), which include the waveguide array (80 waveguides with 200 μm length, the same as the CMT calculations) and input grating coupler that is connected to the interface waveguide. As an example, the scanning electron microscopy (SEM) images of the fabricated structure of $\varphi_0 = 0$, $\Delta\varphi = \pi$ are shown in Figure 2c. In experiments, the light was input into the waveguide lattice by focusing the laser ($\lambda = 1550$ nm) via a grating coupler and a tapered waveguide (see the Experimental Section). The transmitted signals can be collected from the scattered light from the output end by a near-infrared CCD camera (Xenics Xeva-1.7-320). Figure 2d–f (right panels) shows the experimental captured optical signals as light scattered from the output of the arrays with $\Delta\varphi = 0$, $\pi/2$, and π respectively, corresponding to the theoretical designs. As the gauge difference $\Delta\varphi$ increases from 0 to π, the distribution of scattered light at the output gradually gets localized, and eventually to a single spot at the interface, evidently indicating the emergence of localized π-interface modes at $\Delta\varphi = \pi$, which well confirms the CMT and simulation results. We explained the formation of the gauge-induced π modes by analyzing the eigenmode property of π modes in Section S2 of the Supporting Information. It should be noted here that for convenience we only input the light through a single waveguide, which does not strictly conform to the eigenmodes profile of the π interface states. However, theoretical calculations show that this single waveguide input can basically excite this local interface mode as compared with the exact π mode preparations (see Section S3 in the Supporting Information for more details), and does not affect the demonstration of the fundamental physics.

2.3. Influence of Initial Gauge on the π Mode Excitation

Next, we fixed the gauge difference at $\Delta\varphi = \pi$ and change the initial gauge φ_0 ($\varphi_0 = \pi/2$ and π). **Figure 3**a,e shows the zoom-in schematics of input ends for $\varphi_0 = \pi/2$ and π. For $\varphi_0 = \pi/2$ case, there is a bright light spot at the output end that rightly locates at the interface, ensuring the emergence of π-interface mode (see Figure 3d). Surprisingly, for another $\varphi_0 = \pi$ case, we observed an obvious spreading of light at the output end (see Figure 3h) without the π-mode localization. Both experiments are in good coincidence with the CMT and simulation results (see Figure 3b,c and f,g). To explain it, we analyze the eigenmode property of π-interface modes at the initial stage ($z = 0$), as representative distributions shown in Figure 3i,j for $\varphi_0 = \pi/2$ and π, respectively. It is found that localized π-interface modes do exist for both cases, but have different mode profiles. The input waveguide-I (i.e., waveguide #40, marked by dashed red circles) has strong field for $\varphi_0 = \pi/2$ while none for $\varphi_0 = \pi$. This is also true for other π-interface modes (see Section S4 in the Supporting Information). Particularly, we plotted out the intensity of one of the π modes at waveguide-I as a function of φ_0 as shown in Figure 3k.

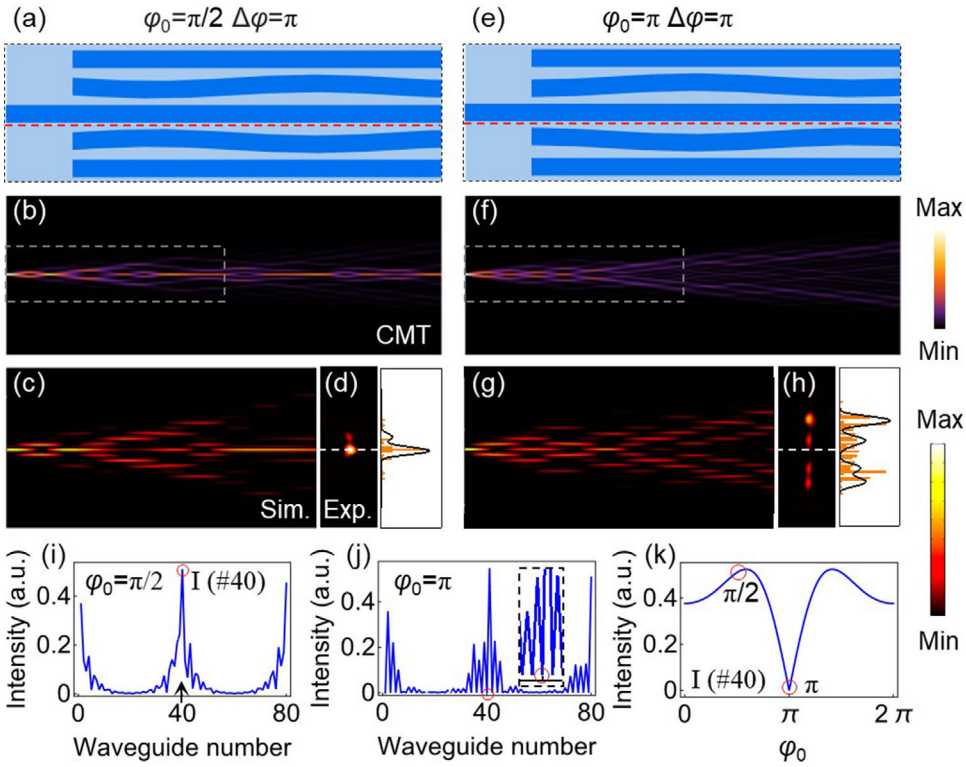

Figure 3. Influence of initial gauge. a–d) $\varphi_0 = \pi/2$, $\Delta\varphi = \pi$. a) Zoom-in schematic of the input end. b) CMT calculated field evolution. c) Simulation result within the boxed region in (b). d) Experimental result with output intensity profiles. e–h) Corresponding results for $\varphi_0 = \pi$, $\Delta\varphi = \pi$. i,j) Field distribution of the π modes at the initial stage ($z = 0$) for $\varphi_0 = \pi/2$ i) and π j), respectively. k) Field intensity of π eigenmodes at waveguide-I with respect to different initial gauge φ_0. The arrow in (i) indicates the interface.

It is evident that π modes have the strongest field at the input waveguide for $\varphi_0 = \pi/2$ but zero at $\varphi_0 = \pi$. Therefore, the input from waveguide-I can excite the π modes to the most extent in the case of $\varphi_0 = \pi/2$ and give rise to robust localization, but not as $\varphi_0 = \pi$ and result in a dispersive feature. This is exactly the experiments have confirmed in Figure 3d,h. Thus, the initial gauge φ_0 influences the excitation condition of the π-interface modes significantly, and more detailed discussions and experimental verifications are provided in Sections S4 and S5 of the Supporting Information.

2.4. Asymmetric Topological Transport by Floquet Gauge Engineering

Inspired by the emergence of gauge-induced π-interface modes and flexible control with gauge modulation, we further explore a function of asymmetric topological transport, which is difficult to achieve in 1D static systems, where one only realizes either the topological transports from both ends or none. Here, we show the feasibility of Floquet gauge system. Specifically, we design a waveguide array with one end to have $\varphi_0 = \pi/2$ (marked by end-A) while the opposite is $\varphi_0 = \pi$ (marked by end-B), as schematically shown in **Figure 4**a. We input light from both ends to examine their propagation properties. Figure 4b,c shows the CMT calculated and experimental results of field evolutions from end-A (forward), respectively. The light propagates along the interface with topologically protected localization according to π-interface modes excitation. However, for the backward case (input from the opposite end-B), no topological mode can be excited and the light will spread out into the entire lattices, as well verified by theory and experiment in Figure 4d,e.

Being energetically isolated from the bulk and strongly confined in real space, the π-interface modes should inherit the topological protection. To examine the robustness of the topological transport, we fabricated controlled samples with random structural discrepancies for comparisons. The theoretical analyses and experimental results are provided in Section S6 of the Supporting Information. It is obvious that for forward propagation, the optical field still propagates along the boundary, which indeed suggests its robustness against disorders. Moreover, we also find that the asymmetric topological transport is considerably insensitive to the wavelengths that indicates a broadband property. Figure 4f shows the extracted normalized output intensity for forward and backward propagations with respect to different wavelengths, which clearly demonstrates the broadband asymmetric topological transport functions. The experimentally measured contrast ratio (determined as $10\log|(I_{A-}I_B)/(I_A+I_B)|$, where $I_{A(B)}$ is the output intensity of the interface lattice sites of end-A(B)) of forward and backward propagations reaches ≈−0.059 dB for central wavelength of 1550 nm, and has a broad band (≈100 nm) for contrast ratio >−1dB (Figure 4g, dashed line). The detailed experimental data can be found in Section S7 of the Supporting Information.

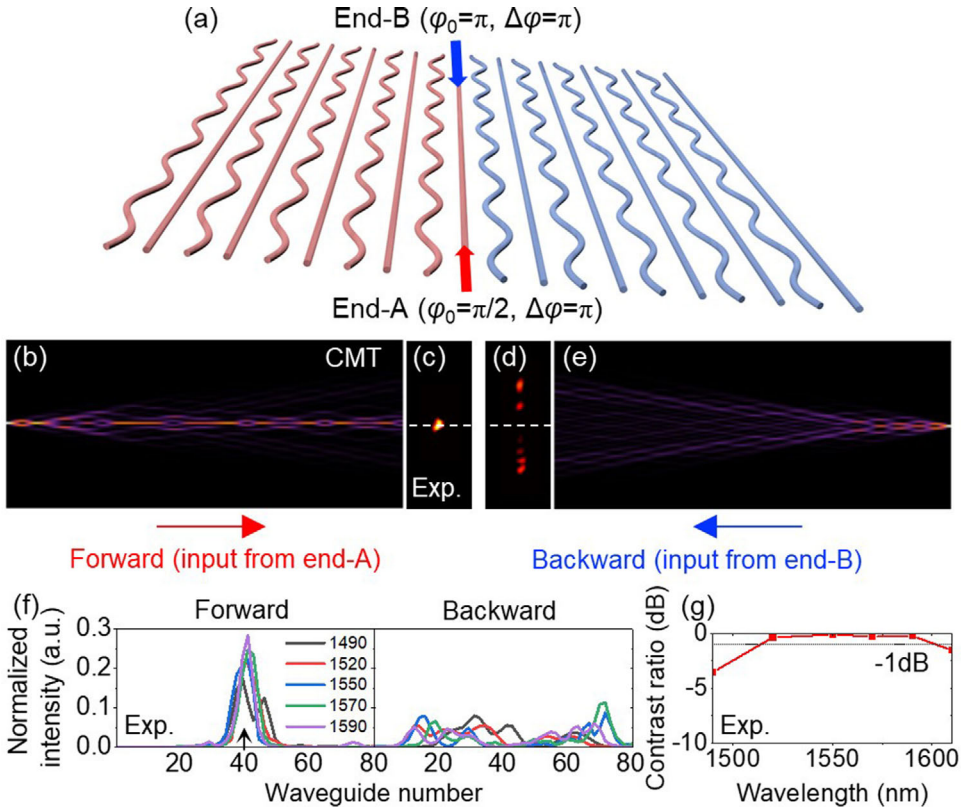

Figure 4. Asymmetric topological transport. a) Schematics of the waveguide array with Floquet gauge modulation at the interface, where end-A and end-B represent the two ends of the waveguide array that have different initial gauges, $\varphi_0 = \pi/2$ for end-A and π for end-B. The red and blue arrows represent input from end-A and end-B, respectively. The length of the waveguide array is 254 μm. b,c) CMT calculated b), experimental detected c) field evolutions with input at end-A for the forward propagation case, showing confined topological transport. d,e) Corresponding results for backward propagation with input from the opposite end-B, showing dispersive feature. f) Normalized output intensity profiles for different wavelengths. g) Contrast ratio for the output fields of forward and backward propagations. The arrow in f) indicates the interface.

3. Discussion and Conclusion

According to bulk-edge correspondence, a topological state is expected to form at an interface between two systems with different topological invariants.[48] However, as we have demonstrated, the two gauge-distinct arrays have the same π-gaps topological invariants of G_π ($G_\pi = 1$, see Figure 1f). Inspired by the Jackiw–Rebbi model,[50–53] it is found that the Floquet gauge is responsible for the contradiction, and the Floquet Hamiltonians of the two gauge-distinct arrays have a π-gap mass term with opposite sign due to the Floquet gauge transition (see Section S8 of the Supporting Information). As such, our gauge-induced interface modes are different from other modulation-induced defect states.[54–56]

In contrast to the topological modes formed at the boundary of a topological domain to a topologically trivial domain (e.g., the zero modes), the gauge-induced topological modes provide us new degrees of freedom in engineering the topological light transport thanks to the gauge modulation, as has been well demonstrated by the asymmetric topological transport experiments by judicious initial gauge design. Compared to the original π modes that can only form at the edges, the gauge-induced π interface modes can be generated inside of the lattices wherever π gauge shift is applied. Notably, the ability to realize topological π transport at will opens the door to many possibilities. For example, the coherent coupling of topological π modes can increase systems versatility and tunability, which has potential in assembling on-chip topological optical devices.[18,57]

In conclusion, we have demonstrated a gauge-induced Floquet state in topological photonic lattices, which arises from the Floquet gauge transition. Thanks to the initial gauge dependence, these π modes can be carefully engineered to access an asymmetric topological transport along the interface with broad working bandwidth and robustness against structural fluctuations. The experiments were implemented in silicon waveguides platform with convincing results fully consistent with the theoretical predictions. Our Floquet gauge engineering enriches new physics in topological photonics systems that give rise to novel optical phenomena and functionalities inaccessible in the static systems.

4. Experimental Section

Sample Fabrication: The waveguide arrays and grating nanostructures are fabricated using the method of electron-beam lithography and ICP etching process. The substrate used herein is 230 nm silicon deposition on 460 μm alumina substrate, and the substrates are cleaned in ultrasound bath in acetone and DI water for 10 min respectively and dried under clean

nitrogen flow. Then 400 nm AR-N7520 photoresist film is spin-coated onto the substrate and baked at 85 °C for 1 min. After that, the sample is exposed to electron beam in E-beam writer (Elionix, ELS-F125) and developed to form the AR-N7520 nanostructures. Then, the sample is transferred into HSE Series Plasma Etcher 200 and etched with C4F8 and SF6 (the flow rates of these two types of gases are 75 sccm:30 sccm). After the ICP etching, the remaining AR-N7520 is removed by using an O_2 plasma for 5 min.

Measurement: In optical measurements, a white light laser (Fianium Super-continuum, 4 W) with the wavelength range from 400 to 2200 nm was used, and the wavelength was switched by a group of filters (FWHM = 12 nm). The light with different wavelength was focused at the input grating by an objective lens (100×), and then coupled into the waveguide mode. The output signals can be detected by the scattering field from the output end by a near-infrared camera (Xeva-1.7-320) through another microscope objective (50×).

Supporting Information

Supporting Information is available from the Wiley Online Library or from the author.

Acknowledgements

The authors acknowledge the financial support from The National Key Research and Development Program of China (2017YFA0303701 and 2016YFA0202103) and the National Natural Science Foundation of China (91850204 and 11674167). Tao Li thanks the support from Dengfeng Project B of Nanjing University.

Conflict of Interest

The authors declare no conflict of interest.

Data Availability Statement

Data available on request from the authors.

Keywords

artificial gauge fields, Floquet states, photonic waveguides, topological photonics

Received: December 23, 2020
Revised: February 24, 2021
Published online:

[1] L. Lu, J. D. Joannopoulos, M. Soljačić, *Nat. Phys.* **2016**, *12*, 626.
[2] T. Ozawa, H. M. Price, A. Amo, N. Goldman, M. Hafezi, L. Lu, M. C. Rechtsman, D. Schuster, J. Simon, O. Zilberberg, I. Carusotto, *Rev. Mod. Phys.* **2019**, *91*, 015006.
[3] W. A. Benalcazar, B. A. Bernevig, T. L. Hughes, *Science* **2017**, *357*, 61.
[4] A. Hassan, F. Kunst, A. Moritz, G. Andler, E. Bergholtz, M. Bourennane, *Nat. Photonics* **2019**, *13*, 697.
[5] S. Mittal, V. V. Orre, G. Zhu, M. A. Gorlach, A. Poddubny, M. Hafezi, *Nat. Photonics* **2019**, *13*, 692.
[6] S. Weimann, M. Kremer, Y. Plotnik, Y. Lumer, S. Nolte, K. G. Makris, M. Segev, M. C. Rechtsman, A. Szameit, *Nat. Mater.* **2017**, *16*, 433.
[7] H. Zhao, X. Qiao, T. Wu, B. Midya, S. Longhi, L. Feng, *Science* **2019**, *365*, 1163.
[8] W. Song, W. Sun, C. Chen, Q. Song, S. Xiao, S. Zhu, T. Li, *Phys. Rev. Lett.* **2019**, *123*, 165701.
[9] G. Harari, M. A. Bandres, Y. Lumer, M. C. Rechtsman, Y. D. Chong, M. Khajavikhan, D. N. Christodoulides, M. Segev, *Science* **2018**, *359*, eaar4003.
[10] M. A. Bandres, S. Wittek, G. Harari, M. Parto, J. Ren, M. Segev, D. N. Christodoulides, M. Khajavikhan, *Science* **2018**, *359*, eaar4005.
[11] Z. Shao, H. Chen, S. Wang, Z. Y. X. Mao, S. Wang, X. Wang, X. Hu, R. Ma, *Nat. Nanotechnol.* **2020**, *15*, 67.
[12] W. P. Su, J. R. Schrieffer, A. J. Heeger, *Phys. Rev. Lett.* **1979**, *42*, 1698.
[13] A. Blanco-Redondo, I. Andonegui, M. J. Collins, G. Harari, Y. Lumer, M. C. Rechtsman, B. J. Eggleton, M. Segev, *Phys. Rev. Lett.* **2016**, *116*, 163901.
[14] Q. Cheng, Y. Pan, Q. Wang, T. Li, S. Zhu, *Laser Photonics Rev.* **2015**, *9*, 392.
[15] S. Xia, D. Jukić, N. Wang, D. Smirnova, L. Smirnov, L. Tang, D. Song, A. Szameit, D. Leykam, J. Xu, Z. Chen, H. Buljan, *Light: Sci. Appl.* **2020**, *9*, 147.
[16] P. St-Jean, V. Goblot, E. Galopin, A. Lemaître, T. Ozawa, L. Le Gratiet, I. Sagnes, J. Bloch, A. Amo, *Nat. Photonics* **2017**, *11*, 651.
[17] H. Zhao, P. Miao, M. H. Teimourpour, S. Malzard, R. El-Ganainy, H. Schomerus, L. Feng, *Nat. Commun.* **2018**, *9*, 981.
[18] W. Song, W. Sun, C. Chen, Q. Song, S. Xiao, S. Zhu, T. Li, *Laser Photonics Rev.* **2020**, *4*, 1900193.
[19] A. P. Slobozhanyuk, A. N. Poddubny, A. E. Miroshnichenko, P. A. Belov, Y. S. Kivshar, *Phys. Rev. Lett.* **2015**, *114*, 123901.
[20] Y. Wu, C. Li, X. Hu, Y. Ao, Y. Zhao, Q. Gong, *Adv. Opt. Mater.* **2017**, *5*, 1700357.
[21] N. H. Lindner, G. Refael, V. Galitski, *Nat. Phys.* **2011**, *7*, 490.
[22] Z. Gu, H. A. Fertig, D. P. Arovas, A. Auerbach, *Phys. Rev. Lett.* **2011**, *107*, 216601.
[23] J. Cayssol, B. Dra, F. Simon, R. Moessner, *Phys. Status Solidi RRL* **2013**, *7*, 101.
[24] Y. T. Katan, D. Podolsky, *Phys. Rev. Lett.* **2013**, *110*, 016802.
[25] D. Leykam, M. C. Rechtsman, Y. D. Chong, *Phys. Rev. Lett.* **2016**, *117*, 013902.
[26] M. S. Rudner, N. H. Lindner, *Nat. Rev. Phys.* **2020**, *2*, 229.
[27] J. K. Asbóth, B. Tarasinski, P. Delplace, *Phys. Rev. B* **2014**, *90*, 125143.
[28] V. Dal Lago, M. Atala, L. E. F. Foa Torres, *Phys. Rev. A* **2015**, *92*, 023624.
[29] M. Fruchart, *Phys. Rev. B* **2016**, *93*, 115429.
[30] Q. Cheng, Y. Pan, H. Wang, C. Zhang, D. Yu, A. Gover, H. Zhang, T. Li, L. Zhou, S. Zhu, *Phys. Rev. Lett.* **2019**, *122*, 173901.
[31] S. Mukherjee, A. Spracklen, M. Valiente, E. Andersson, O. Ohberg, N. Goldman, R. R. Thom- son, *Nat. Commun.* **2017**, *8*, 13918.
[32] L. J. Maczewsky, J. M. Zeuner, S. Nolte, A. Szameit, *Nat. Commun.* **2017**, *8*, 13756.
[33] A. Kundu, B. Seradjeh, *Phys. Rev. Lett.* **2013**, *111*, 136402.
[34] D. T. Liu, J. Shabani, A. Mitra, *Phys. Rev. B* **2019**, *99*, 094303.
[35] A. C. Potter, T. Morimoto, A. Vishwanath, *Phys. Rev. X* **2016**, *6*, 041001.
[36] D. V. Else, C. Nayak, *Phys. Rev. B* **2016**, *93*, 201103.
[37] M. Bukov, L. D'Alessio, A. Polkovnikov, *J. Adv. Phys.* **2015**, *64*, 139.
[38] A. Eckardt, E. Anisimovas, *New J. Phys.* **2015**, *17*, 093039.
[39] K. Fang, K. Z. Yu, S. Fan, *Nat. Photonics* **2012**, *6*, 782.
[40] M. Hafezi, E. A. Demler, M. D. Lukin, J. M. Taylor, *Nat. Phys.* **2011**, *7*, 907.
[41] M. C. Rechtsman, J. M. Zeuner, Y. Plotnik, Y. Lumer, D. Podolsky, F. Dreisow, S. Nolte, M. Segev, A. Szameit, *Nature* **2013**, *496*, 196.
[42] M. Hafezi, S. Mittal, J. Fan, A. Migdall, J. M. Taylor, *Nat. Photonics* **2013**, *7*, 1001.
[43] S. Longhi, M. Marangoni, M. Lobino, R. Ramponi, P. Laporta, E. Cianci, V. Foglietti, *Phys. Rev. Lett.* **2006**, *96*, 243901.

[44] A. Szameit, I. L. Garanovich, M. Heinrich, A. A. Sukhorukov, F. Dreisow, T. Pertsch, S. Nolte, A. Tünnermann, Y. S. Kivshar, *Nat. Phys.* **2009**, *5*, 271.
[45] W. Song, H. Li, S. Gao, C. Chen, S. Zhu, T. Li, *Adv. Photonics* **2020**, *2*, 036001.
[46] Q. Lin, S. Fan, *Phys. Rev. X* **2014**, *4*, 031031.
[47] Y. Lumer, M. A. Bandres, M. Heinrich, L. J. Maczewsky, H. Herzig-Sheinfux, A. Szameit, M. Segev, *Nat. Photonics* **2019**, *13*, 339.
[48] X. Qi, Y. Wu, S. Zhang, *Phys. Rev. B* **2006**, *74*, 045125.
[49] I. L. Garanovich, S. Longhi, A. A. Sukhorukov, Y. S. Kivshar, *Phys. Rep.* **2012**, *518*, 1.
[50] R. Jackiw, C. Rebbi, *Phys. Rev. D* **1976**, *13*, 3398.
[51] J. Goldstone, F. Wilczek, *Phys. Rev. Lett.* **1981**, *47*, 986.
[52] D. G. Angelakis, P. Das, C. Noh, *Sci. Rep.* **2014**, *4*, 6110.
[53] T. X. Tran, F. Biancalana, *Phys. Rev. A* **2017**, *96*, 013831.
[54] I. L. Garanovich, A. A. Sukhorukov, Y. S. Kivshar, *Phys. Rev. Lett.* **2008**, *100*, 203904.
[55] A. Szameit, I. L. Garanovich, M. Heinrich, A. A. Sukhorukov, F. Dreisow, T. Pertsch, S. Nolte, A. Tünnermann, Y. S. Kivshar, *Phys. Rev. Lett.* **2008**, *101*, 203902.
[56] B. Zhu, H. Zhong, Y. Ke, X. Qin, A. A. Sukhorukov, Y. S. Kivshar, C. Lee, *Phys. Rev. A* **2018**, *98*, 013855.
[57] Y. Wang, W. Liu, Z. Ji, G. Modi, M. Hwang, R. Agarwal, *Nano Lett.* **2020**, *20*, 8796.